CrossMark

ORIGINAL ARTICLE

Influence of the machine tool compliance on the dynamic performance of the servo drives

Igor Ansoategui[1] · Francisco J. Campa[2] · Carolina López[2] · Mikel Díez[2]

Abstract The development of large machinery in the industry of the machine tool implies moving heavy structural components and pieces. The consequence is the apparition of inaccuracies at the tool tip during the motion due to the high inertial forces acting on the compliant machine. To predict the dynamic behavior of these machines, a three degree of freedom mechatronic model has been developed considering the dynamics of the transmission chain of the drive, the machine structural element dynamics, and the control. The model can be used in the design stage to estimate the maximum jerk that can be commanded without the appearance of overshoot at the tool tip. Also, it can be used to predict the bandwidth of the whole mechatronic system. The model has been tested in a ball screw-based test bench with a compliant mass that simulates the structural compliance of a real large machine tool.

✉ Igor Ansoategui
igor.ansoategui@ehu.eus

Francisco J. Campa
fran.campa@ehu.eus

Carolina López
clugarte07@gmail.com

Mikel Díez
mikel.diez@ehu.eus

[1] Mechanical Engineering Department, University College of Engineering Vitoria-Gasteiz, University of the Basque Country UPV/EHU, Nieves Cano, 12, 01006 Vitoria-Gasteiz, Spain

[2] Mechanical Engineering Department, Bilbao Faculty of Engineering, University of the Basque Country UPV/EHU, Alameda de Urquijo, s/n, 48013 Bilbao, Spain

Nomenclature

|	
ϕ_i	Eigenvector or deformation mode
c_{em}	Damping coefficient in the motor shaft
c_{AF1}	Damping coefficient of the first half in the flexible coupling
c_{AF2}	Damping coefficient of the second half in the flexible coupling
c_{Ht}	Torsional damping coefficient in the screw shaft
c_{Ha}	Axial damping coefficient in the screw shaft
c_T	Damping coefficient in the nut
c_M	Damping coefficient in the table
c_C	Damping coefficient in the column
k_{aT}	Nut axial stiffness
k_{aS}	Nut support axial stiffness
k_{ft}	Bending stiffness of the screws that attach the nut support to the table
k_b	Bearing stiffness
k_{fb}	Thrust bearing stiffness
k_{Ha1}	Axial screw stiffness on the side between the table and thrust bearing
k_{Ha2}	Axial screw stiffness on the opposite side between the table and bearing
τ_d	Disturbance torque
$\dot{\theta}_M$	Real angular velocity of the motor
τ_{Fc}	Coulomb friction force torque

1 Introduction

In the recent years, the rise of renewable energy sectors, railroad, aviation, marine platforms, fusion energy in large scientific plants, etc. has required the development of large machine tools. The main challenge for the designers is to guarantee the precision of the tool tip motion in the whole workspace, due to their high weight and the use of large cantilevered structural

elements as columns or rams. As a consequence, several problems appear. For example, these machines have low natural frequencies, which mean that they suffer from chatter during the milling [1]. They also need to be calibrated in a very large workspace to compensate for deflections due to their own weight [2]. Also, thermal problems are present and must be compensated, especially in machines that work in tropical climates under relatively high gradients of ambient temperature [3]. Finally, the combination of low natural frequencies and high inertial forces complicates the position control of the tool tip when the machine attempts to perform complex movements [2].

This work is focused on the last problem, that is, the position control of the tool tip for large machines. In these machines, the location of the encoders used for the position control is far away from the tool tip, see Fig. 1, which means that the deflection of the structural elements due to the inertial forces results in a tracking error that must be minimized. This can be done from the design stage, using mechatronic models to analyze the mechanical transmission and structure dynamic performance.

For a simple mechatronic analysis of servo drives, inertial models can be used [4]. However, in order to consider the flexibility of the transmission chain, the most common approach is to develop models with two degrees of freedom (dof). Over the recent decades, various mechatronic models of two dof, angular position at the motor encoder and position at the linear encoder, have been developed. Among others, A. Dequidt [5] in 2000 developed a model of two dof, with new rules for determining the bandwidth and the inertial ratio. Y. Altintas [6] in 2011 conducted a comprehensive review of the design and control of drive systems, and more recently, R. Caracciolo [7] in 2014 proposes a new mechatronic model
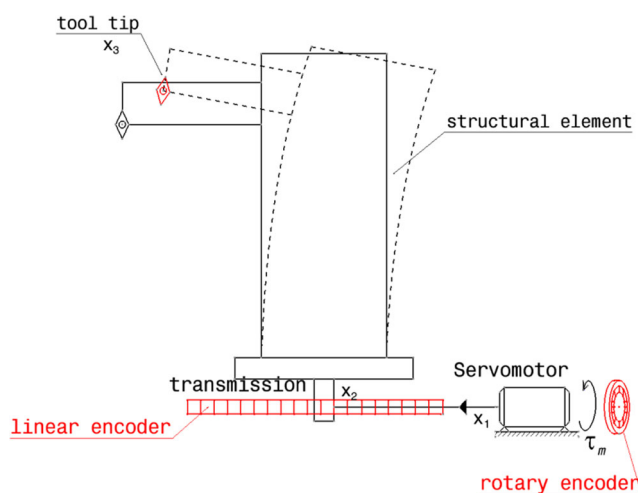
that minimizes the torque of the motor. However, for large machine tools with a large inertia and limited stiffness in the elements of the machine, two dof models are not precise enough. A third dof must be added for the tool tip as in Fig. 1 modeling the compliant nature of the structural elements located from the linear encoder to the tool tip. If not, high overshoots will be obtained at the end of the column or ram where the tool tip is.

Among the authors who have developed three dof mechatronic models, R. Neugebauer [8] presents an optimization of large machines behavior to achieve higher accelerations thus reducing the machining process time. Wu S. T. [9] built a prototype based on a compliant beam over a ball screw drive, using noise filters and a linear enhancer to control the vibration during the motion. A. Fortunato [10] designed a virtual model of machining centers, based on the approximation of lumped mass and a finite element method. This virtual model helps the designer in the optimum definition of the characteristics of the machine tool.

The present work presents a three dof mechatronic model of a general drive and analyzes the influence of the commanded jerk from the NC on the position error on the linear encoder and the tool tip of the machine. Zulaika and Altamira [11] demonstrated that the impact of the jerk on the overshoot depends heavily on the natural frequency of the transmission using a two dof model. Here, the three dof model has been used to quantify the influence of the jerk on the overshoot considering the flexibility of the structural elements of the machine. The analysis has been experimentally validated simulating the machine tool compliance in a test bench with a mass located over two thin cantilever plates attached to a ball screw drive table.

First, in Section 2, the dynamic and mechatronic three dof model will be presented comparing it with a two dof model and calculating the corresponding transfer functions. In Section 3, the influence of structural flexibility on the position error in tool tip and the maximum commanded jerk are analyzed. Section 4 is a case study where the modeling is applied to the test bench, characterizing all the dynamic parameters, and calculating the modal frequencies and transfer functions. Finally, in Section 5, it is presented in an experimental validation with the time response of the test bench under several jerk conditions.

Fig. 1 Influence of the column flexibility on the tool tip error. x_1 motor encoder position, x_2 linear encoder measured position, x_3 tool tip real position

2 Modeling

To develop the three dof mechatronic model, first, it is necessary to analyze the three dof dynamic model of the plant.

2.1 Dynamic modeling

In Fig. 2, the two and three dof-lumped parameters models are shown, connecting lumped masses by springs and dampers. This is a well-known approach to dynamic modeling of an electromechanical drive [12, 13].

In the two dof model of Fig. 2, x_1 is the position of the motor and x_2 is the position of the load (tool tip) measured at the linear encoder. In the three dof model, x_1 is the same, x_2 is the position measured at the linear encoder, and x_3 is the tool tip position. The mass m_1 represents the motor inertia, the second mass m_2 is the transmission inertia for the b case, and the transmission and load for the a case. The third mass m_3 represents the inertia of the compliant structure in the b case. k and c represent the transmission stiffness and damping of the two dof model. Respectively, k_1 and c_1 are the stiffness and damping of the transmission chain from the motor to the linear encoder and k_2 and c_2 the stiffness and damping of the structural element from the linear encoder to the tool tip. Moreover, for both models, the f force is equivalent to the servomotor torque, f_d is the disturbance force due to friction and cutting forces, and c_m is the viscous damping of the motor. The latter two terms will be considered as an external disturbance torque.

The model equations can be found using the principle of D'Alembert, the virtual works principle, energy theorem, the Lagrange equations [14], or Newton's second law. In this study, following the Newton approach, the matrix form of the motion equation of two dof model is

$$
\begin{bmatrix} m_1 & 0 \\ 0 & m_2 \end{bmatrix} \cdot \begin{Bmatrix} \ddot{x}_1 \\ \ddot{x}_2 \end{Bmatrix} + \begin{bmatrix} c & -c \\ -c & c \end{bmatrix} \cdot \begin{Bmatrix} \ddot{x}_1 \\ \ddot{x}_2 \end{Bmatrix}
$$
$$
+ \begin{bmatrix} k & -k \\ -k & k \end{bmatrix} \cdot \begin{Bmatrix} x_1 \\ x_2 \end{Bmatrix}
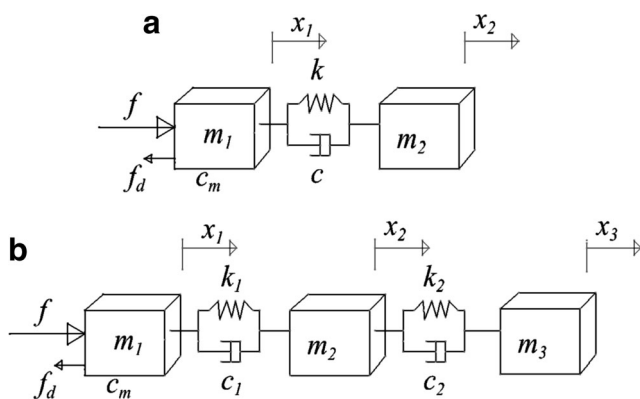$$
$$
= \begin{Bmatrix} f \\ 0 \end{Bmatrix}. \tag{1}
$$

Fig. 2 Lumped parameters scheme. **a** Two dof model. **b** Three dof model

From the modal analysis, there are two modal frequencies. The first is null because it represents the rigid body mode. The second is

$$
\omega_2 = \sqrt{\frac{k(m_1 + m_2)}{m_1 \cdot m_2}}. \tag{2}
$$

The matrix form of the motion equation of three dof model is

$$
\begin{bmatrix} m_1 & 0 & 0 \\ 0 & m_2 & 0 \\ 0 & 0 & m_3 \end{bmatrix} \begin{Bmatrix} \ddot{x}_1 \\ \ddot{x}_2 \\ \ddot{x}_3 \end{Bmatrix}
$$
$$
+ \begin{bmatrix} c_1 & -c_1 & 0 \\ -c_1 & c_1 + c_2 & -c_2 \\ 0 & -c_2 & c_2 \end{bmatrix} \begin{Bmatrix} \ddot{x}_1 \\ \ddot{x}_2 \\ \ddot{x}_3 \end{Bmatrix}
$$
$$
+ \begin{bmatrix} k_1 & -k_1 & 0 \\ -k_1 & k_1 + k_2 & -k_2 \\ 0 & -k_2 & k_2 \end{bmatrix} \begin{Bmatrix} x_1 \\ x_2 \\ x_3 \end{Bmatrix}
$$
$$
= \begin{Bmatrix} f \\ 0 \\ 0 \end{Bmatrix}. \tag{3}
$$

From the equations of motion of the two and three dof models, the Laplace transform is developed.

As in the two dof model, the first modal frequency is zero, and the second and third mode frequencies are the following:

$$
\omega_2 = \sqrt{\frac{1}{2}\left((\omega_{123})^2 - \sqrt{\left((\omega_{123})^4 - 4k_1k_2\left(\frac{m_T}{m_1m_2m_3}\right)\right)}\right)}.
$$
$$
\omega_3 = \sqrt{\frac{1}{2}\left((\omega_{123})^2 + \sqrt{\left((\omega_{123})^4 - 4k_1k_2\left(\frac{m_T}{m_1m_2m_3}\right)\right)}\right)}. \tag{4}
$$

The m_T term of Eq. (4) corresponds to the sum of the three mass systems. The ω_{123} frequency depends on the natural frequencies resulting from fixing 2 of the 3 degrees of freedom alternatively:

$$
(\omega_{123})^2 = \left(\frac{k_1}{m_1} + \frac{k_1 + k_2}{m_2} + \frac{k_2}{m_3}\right)
$$
$$
= (\omega_{1r23})^2 + (\omega_{2r13})^2 + (\omega_{3r12})^2 \tag{5}
$$

From the motion equations, after passing them to the frequency domain, the dynamic of the drive is here modeled by transfer functions, although the state space approach can be also used [12]. It is defined as the primary transfer function TF_1, the one that relates the angular position of the motor in the encoder with the motor torque. The secondary transfer function TF_2 relates the linear encoder position with the motor angular position. Finally, the tertiary transfer function TF_3

relates the tool tip position with the linear encoder position. The transfer functions are represented by Eq. (6) whose coefficients are shown in Table 1 for two and three dofs.

$$TF_i = \frac{n_4 s^4 + n_3 s^3 + n_2 s^2 + n_1 s + n_0}{d_6 s^6 + d_5 s^5 + d_4 s^4 + d_3 s^3 + d_2 s^2 + d_1 s + d_0}. \quad (6)$$

Also, the modal analysis of the three dof model has been performed to find in symbolic way to relate the damping coefficients with the damping ratios in the three dof model, which is explained in Section 2.1.1. The modal matrix of the three dof model is provided by Blevins [15], and here, in Appendices 1–3, it is shown that the mass normalized modal matrix necessary for the damping calculation.

2.1.1 Damping

From the characteristic equation associated with a plant of a two dof model, the damping coefficient of the system is related to the damping ratio ξ_2 as

$$c = 2\xi_2 \omega_2 \frac{m_1 m_2}{m_1 + m_2}. \quad (7)$$

In a three dof model, the damping coefficient matrix $[C]$ converted to modal coordinates and assuming proportional damping is:

$$[\phi]^T [C][\phi] = \begin{bmatrix} 0 & 0 & 0 \\ 0 & 2\xi_2 \omega_2 & 0 \\ 0 & 0 & 2\xi_3 \omega_3 \end{bmatrix}. \quad (8)$$

Taking into account the normalized modal matrix of Eq. (18) in Appendix 1, Eq. (8) gives the relation between the two damping coefficients of the three dof model, c_1 and c_2.

$$c_2 = \frac{c_1 \left(-\omega_{3r12}^4 + \omega_2^2 \omega_{3r12}^2 + \omega_3^2 \omega_{3r12}^2 - \omega_2^2 \omega_3^2 \right)}{\left(\omega_2^2 - \omega_{1r23}^2 \right)\left(\omega_3^2 - \omega_{1r23}^2 \right)}. \quad (9)$$

Also, it provides the relation with the damping ratios in the three dof system:

$$\xi_2 = \frac{c_1 \omega_2^3 \left(\omega_2^2 - \omega_3^2 \right)\left(\omega_2^2 - \omega_{3r12}^2 \right)\left(\omega_{3r12}^2 - \omega_{1r23}^2 \right)}{2\left(\omega_3^2 - \omega_{1r23}^2 \right)\left(m_3 \omega_{3r12}^4 \left(\omega_2^2 - \omega_{1r23}^2 \right)^2 + m_1 \left(\omega_2^2 - \omega_{3r12}^2 \right)^2 \omega_{1r23}^4 + m_2 \left(\omega_2^2 - \omega_{3r12}^2 \right)^2 \left(\omega_2^2 - \omega_{1r23}^2 \right)^2 \right)}.$$

$$\xi_3 = \frac{c_1 \omega_3^3 \left(\omega_3^2 - \omega_2^2 \right)\left(\omega_3^2 - \omega_{3r12}^2 \right)\left(\omega_{3r12}^2 - \omega_{1r23}^2 \right)}{2\left(\omega_2^2 - \omega_{1r23}^2 \right)\left(m_3 \omega_{3r12}^4 \left(\omega_3^2 - \omega_{1r23}^2 \right)^2 + m_1 \left(\omega_3^2 - \omega_{3r12}^2 \right)^2 \omega_{1r23}^4 + m_2 \left(\omega_3^2 - \omega_{3r12}^2 \right)^2 \left(\omega_3^2 - \omega_{1r23}^2 \right)^2 \right)}. \quad (10)$$

Table 1 Transfer function numerator and denominator coefficients in natural coordinates

	$TF_1 = \frac{x_1}{f}$		$TF_2 = \frac{x_2}{x_1}$		$TF_3 = \frac{x_3}{x_2}$
	2 dof	3 dof	2 dof	3 dof	3 dof
n_0	k	$k_1 k_2$	k	$k_1 k_2$	k_2
n_1	c	$c_1 k_2 + c_2 k_1$	c	$c_1 k_2 + c_2 k_1$	c_2
n_2	m_2	$m_3 k_1 + (m_2 - m_3)k_2 + c_1 c_2$	0	$m_3 k_1 + c_1 c_2$	0
n_3	0	$m_3 c_1 + (m_2 - m_3)c_2$	0	$m_3 c_1$	0
n_4	0	$m_2 m_3$	0	0	0
d_0	0	0	k	$k_1 k_2$	k_2
d_1	0	0	c	$c_1 k_2 + c_2 k_1$	c_2
d_2	$(m_1 + m_2)k$	$(m_1 + m_2 - m_3)k_1 k_2$	m_2	$m_3 k_1 + (m_2 - m_3)k_2 + c_1 c_2$	m_3
d_3	$(m_1 + m_2)c$	$(m_1 + m_2 - m_3)(c_2 k_1 + c_1 k_2)$	0	$m_3 c_1 + (m_2 - m_3)c_2$	0
d_4	$m_1 m_2$	$(m_1 + m_2)m_3 k_1 + (m_2 - m_3)m_1 k_2 + (m_1 + m_2 - m_3)c_1 c_2$	0	$m_2 m_3$	0
d_5	0	$(m_1 + m_2)m_3 c_1 + (m_2 - m_3)m_1 c_2$	0	0	0
d_6	0	$m_1 m_2 m_3$	0	0	0

2.1.2 Friction perturbation

Considering the friction as the only source of disturbance, the viscous damping c_m, and the Coulomb friction torque τ_{fc}, the disturbance torque in the models is

$$\tau_{f_d} = c_m \cdot \dot{\theta}_M + \tau_{f_c}. \tag{11}$$

Those two values can be determined by measuring motor torque for several constant feed rates and performing a linear regression vs. motor speed [16, 17].

2.2 Mechatronic model

The mechatronic model integrates the plant dynamics, control, and sensor performance. The model is shown in Fig. 3, where the position and the velocity control loops with their cycle times are modeled and the tertiary transfer function is located after the closed position loop.

System belongs to a servo drive that is added a compliant mass as shown in Fig. 1. Regarding the control, it is the usual PID cascade control of position, speed, and intensity. Position control is based on a proportional controller P with a feed forward (FFV) added. The velocity control has a PI controller as well as the current control. Nevertheless, the current loop is modeled only with constant torque as it runs with a cycle time much faster than the speed and position control loops, because the dynamics of electrical phenomena will be faster than mechanical for large machine tools. It is worth noting that there is no direct control of the tool tip position as it usually happens with machine tools.

To adapt to the shape of the mechatronic model shown in Fig. 1, the angular position can be related to the linear position through a screw pitch p, in the case of a ball screw drive. Also, the conversion between torque and force must be solved. So, the resulting transfer functions are the following:

$$TF'_1 = \frac{\omega_m}{\tau_m} = \frac{x_1}{f}\left(\frac{2\pi}{p}\right)^2 s = TF_1 \left(\frac{2\pi}{p}\right)^2 s.$$
$$TF'_3 = TF_3 = \frac{x_3}{x_2}.$$

$$TF'_2 = \frac{x_2}{\omega_m} = \frac{x_2}{x_1}\left(\frac{p}{2\pi}\right)\frac{1}{s} = TF_2 \left(\frac{p}{2\pi}\right)\frac{1}{s}. \tag{12}$$

The "s" term used in the first two transfer functions of Eq. (12) represents the Laplace variable.

For tertiary transfer function, there is no need of any changes as it directly has the relation between flexible mass positions with table position. Obviously, for the two dof model study, tertiary transfer function is excluded.

3 Structural flexibility influence on the tool tip position error and the maximum commanded jerk

One way to quantify the influence of the jerk in the propagation of the motion from the motor to the tool tip through the transmission is to analyze the temporal response of the two and the three dof models. Assuming the motor describe a sine
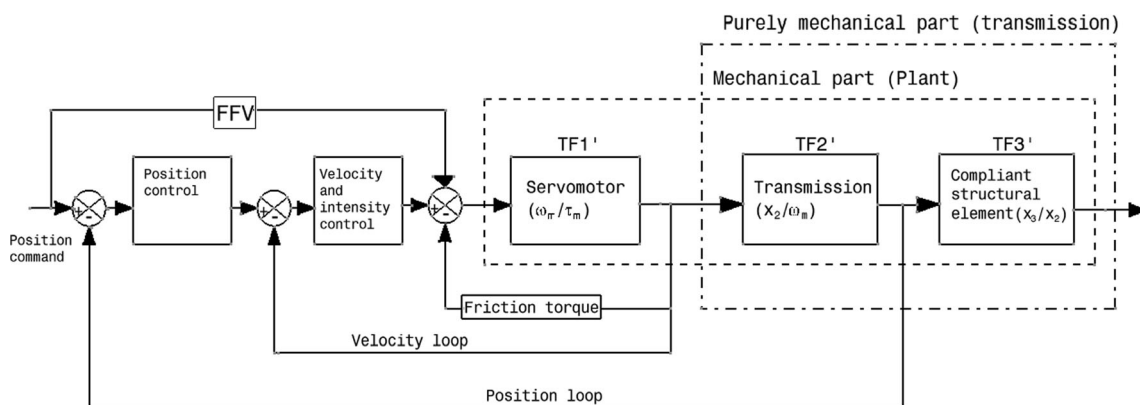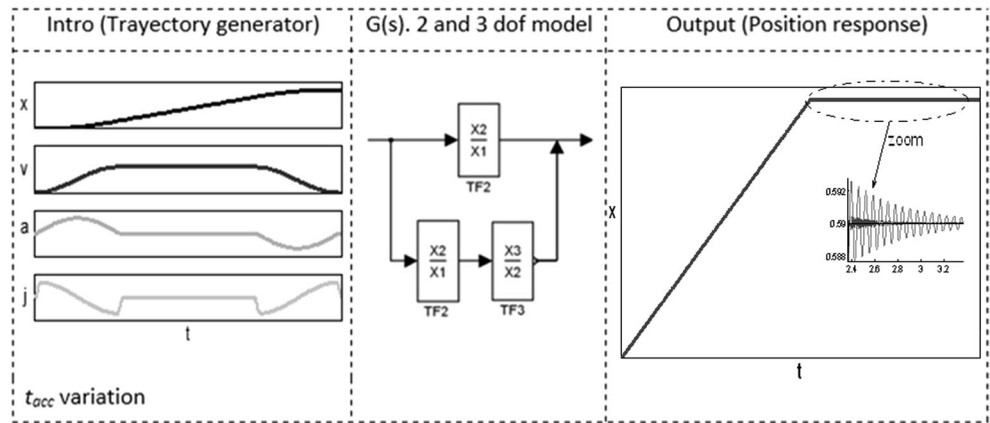

Fig. 3 Three dof mechatronic model of a compliant machine tool drives

Fig. 4 A position command diagram

square path x_1, here, it will be seen how the transmission at the linear encoder x_2 and the tool tip x_3 follow that motion. This analysis has been done initially under the open loop hypothesis. To perform this analysis, a motor path generator with increasing jerk has been programmed in Simulink defining TF_2 and TF_3 transfer functions as in Section 2.1, see Fig. 4. The time response of x_2 and x_3 will be compared to x_1 to calculate the tracking errors focusing especially on the overshoot. In the case of a three dof model, the compliance of the structure will cause a different overshoot between x_2 and x_3. To change the jerk between simulations, the acceleration time t_{acc}, which will define the slope of the speed command curve, will be changed.

The main figure of Fig. 5 orients the tendency of the overshoot when the maximum commanded jerk increases for different cases of rigidities ratio k_2/k_1. On the other hand, in the sub graph window, overshoots and jerks are detailed, this time comparing only a three dof model case ($k_2 = 0.01*k_1$) and the two dof model.

In the window of Fig. 5, it is shown that in the two dof model for 15 μm of overshoot, the maximum commanded jerk must be 680 m/s^3. For the three dof model, it is noted that there are many intersections between the 15 μm line and the curve, so there is not only one value for the commanded maximum jerk for 15 μm of overshoot. But the most conservative jerk is 30 m/s^3. Between 30 m/s^3 and 680 m/s^3, there is an error of 95.59 %. Therefore, the maximum error in the commanded jerk estimation when the elasticity of the structural element is ignored, exceeds 95 % in this example ($k_2 = 0.01*k_1 = 1 \%*k_1$).

In the experience of the authors and after consulting with the manufacturers of large machine tools, the maximum commanded jerk is usually between the 15 and 30 m/s^3 and agree with the values that have been studied.

4 Case study

A test bench has been set up as shown in Fig. 6. It consists of a servomotor Fagor 42.30 A FKM with a nominal torque of 6.3 Nm, a Korta KBS-3210 ball screw with an outer diameter of 32 mm and a pitch of 10 mm with a single nut and a flange, and a Heidenhain Ls 186 MI640 linear encoder with 0.5 μm of resolution. The drive is controlled by a Fagor 8035 NC, which has an oscilloscope function that allows measuring position at the motor and linear encoder, tracking error, and

Fig. 5 Overshoot vs. jerk, two dof, and three dof
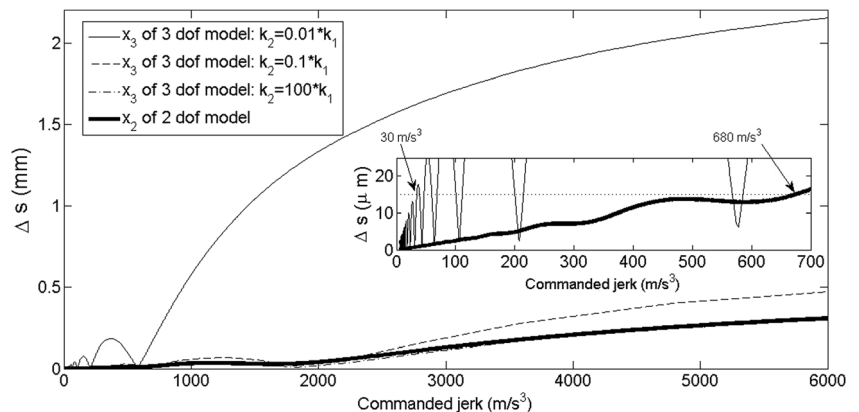
Fig. 6 Test bench with a compliant mass over a ball screw drive
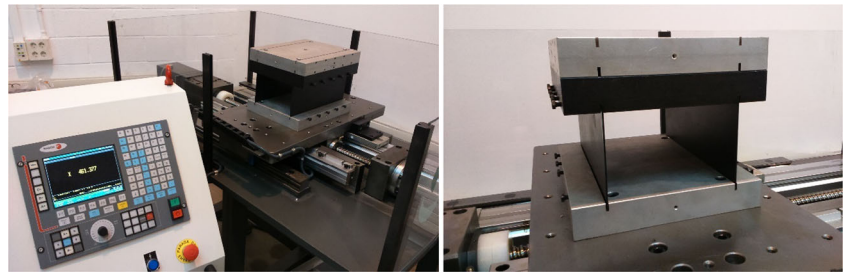
motor torque. The cycle times are 4 ms for the position loop, and 62.5 μs for the of the velocity loop. On top of the table of the drive, two cantilever thin plates of steel have been setup with a mass of 30 kg above, which will be considered as the tool tip position. Concerning the natural frequencies of the machine tools, the dominant structural natural frequency is in the range of 10–100 Hz, while in large machines is between 3 and 15 Hz [2]. The prototype of our case has a structural natural frequency around 15 Hz.

4.1 Transmission chain elements inertia and stiffness characterization

The drive components rigidities have been modeled using the standard formulation of elasticity theory, Eq. (20) of Appendix 2. The resulting rigidities of some element have been calculated with Eqs. (21) and (22) of the Appendix 3 and listed in Table 2, assuming that the union nut-carriage is located in the middle of the axis. The remaining rigidities have been provided by the manufacturers as indicated. Inertias are also calculated with Eqs. (23), (24), and (25) of Appendix 3 and listed below.

As Magnani et al. [18] propose, here, first the lumped parameters of all the components have been coupled in series, thus providing an eight dof dynamic model as shown in Fig. 7a. The degrees of freedom are servomotor position θ_0,

flexible coupling first half position θ_1, flexible coupling second half position θ_2, screw section at the nut angular and linear position θ_3 and x_2, nut position x_2, table s_1, and flexible mass position $s_{1'}$. For simplicity's sake, that model has been reduced to the three dof model here studied, see Fig. 7b.

In order to obtain the screw equivalent axial stiffness, the shaft stiffness k_{Ha1} on the side between the table and the thrust bearing stiffness k_{fb}, will be added to the rigidity of the opposite side k_{Ha2} and k_b according to the distribution of Fig. 7.

$$k_{Ha} = \frac{k_{fb} \cdot k_{Ha1}}{k_{fb} + k_{Ha1}} + \frac{k_b \cdot k_{Ha2}}{k_b + k_{Ha2}} \tag{13}$$

With Eq. (14), the calculation of stiffness is explained by the displacement of the table, where table-nut-screw joint has influence. The flange of the nut is axially fixed with five screws to a support nut, and the nut is fixed vertically by four screws to the table. The first screws affect only structurally, but the vertical screws may flex so may influence in the transmission. The resulting transmission stiffness of this link will be

$$\frac{1}{k_M} = \frac{1}{k_{aT}} + \frac{1}{k_{aS}} + \frac{1}{4 \cdot k_{ft}}. \tag{14}$$

All rigidities of Table 2, except the columns one, represent k_1 of the three dof model, see Fig. 7. The stiffness of the thin plates is k_2.

Table 2 Components' rigidities, inertias and equivalences to the three dof model

		Components stiffness	Equivalent stiffness (N/m)	Components inertia and masses	Equivalent mass (kg)
Motor shaft		$k_{em} = 3.23 \cdot 10^4 Nm/rad$	$k_1 = 5.362.10^7$	$*J_m = 8.5 \cdot 10^{-4} kg \cdot m^2$	$m_1 = 335.57$
Coupling		$*k_{AF} = 4.01 \cdot 10^3 Nm/rad$		$*J_{AF1} = J_{AF2} = 8.53 \cdot 10^{-5} kg \cdot m^2$	$m_2 = 392.97$
Ball	Torsion	$k_{Ht} = 1.72 \cdot 10^4 Nm/rad$		$*J_H = 6.25 \cdot 10^{-4} kg \cdot m^2$	
screw	Axial	$k_{Ha} = 1.23 \cdot 10^8 N/m$			
Nut		$*k_T = 5.45 \cdot 10^8 N/m$		$*m_T = 1.23\ kg$	
Table		$k_M = 6.29 \cdot 10^7 N/m$		$*m_M = 68.5\ kg$	
Column		$**k_C = 3.7060 \cdot 10^4 N/m$		$**m_C = 4.228\ kg$	$m_3 = 4.2280$
			$k_2 = 3.7060.10^4$		

*Provided by the manufacturers

**Calculated by modal analysis
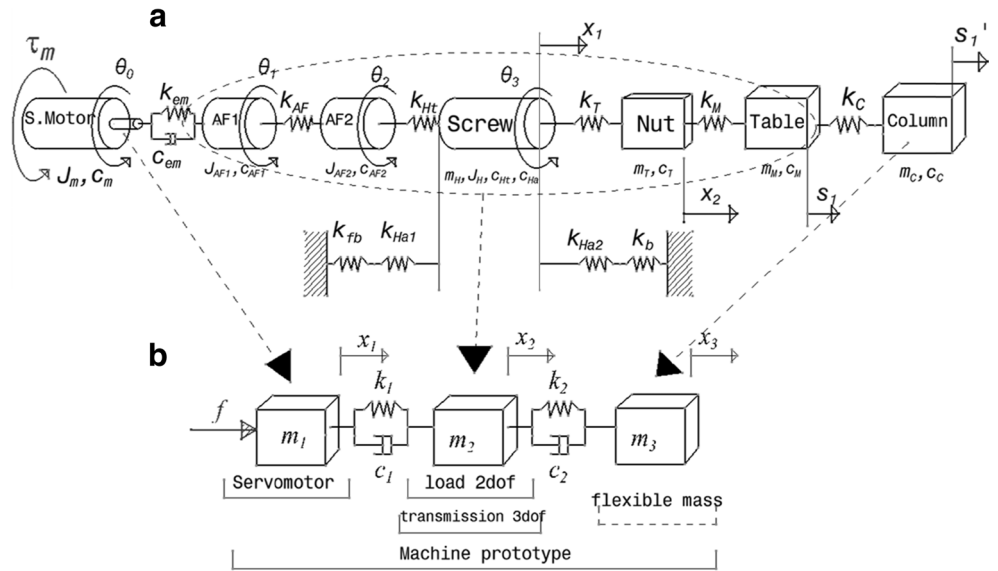
4.2 Experimental characterization

4.2.1 Experimental characterization of the damping and disturbance in the drive

Following the steps of Section 2.1.2 and considering the experimental perturbations and the regression curve $\tau_{fC} = 2.2$ Nm and $c_m = 0.0076$ Nms are obtained. These values of friction and viscous friction damping will be introduced in the disturbance torque block of the mechatronic model, as in Fig. 3.

4.2.2 Experimental characterization of the flexible element

The characterization of the flexible element allows to quantify the mass, stiffness, and damping of the thin plates and the mass. The experimental modal analysis has been done with an impact test with the aid of a hammer 086c03 PCB, a small mass teardrop accelerometer PCB 352C22 with 10.44 mV/g of sensitive, a OROS OR35 signal analyzer with four channels, and a OROS NV Gate acquisition program. Subsequently, in MATLAB transfer function as well as the phase and the real and imaginary plots, it is obtained, as shown below in Fig. 8.

The results of Fig. 8 show that the natural frequency is $f_2 = 14.9$ Hz. The two peaks of the real part of the transfer function are produced in $f_{21} = 15.63$ Hz and $f_{22} = 14.38$ Hz. Therefore, the frequency is increased $\Delta f = 1.25$ Hz, and the relative damping of the flexible mass of the prototype gives $\xi_3 = \frac{\Delta f}{f_2} = 0.0839$.
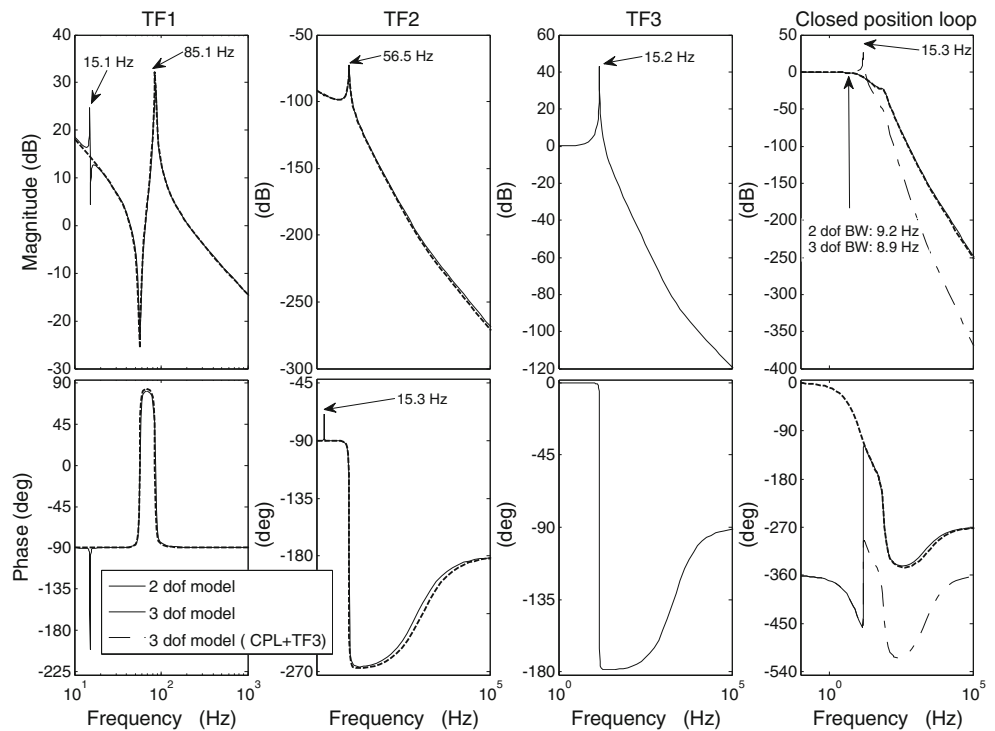
The minimum value of the imaginary part determines the rigidity of the flexible element as

Fig. 8 Results of experimental modal analysis on the flexible mass characterization. **a** Transfer function Bode. **b** Real and imaginary part of the transfer function
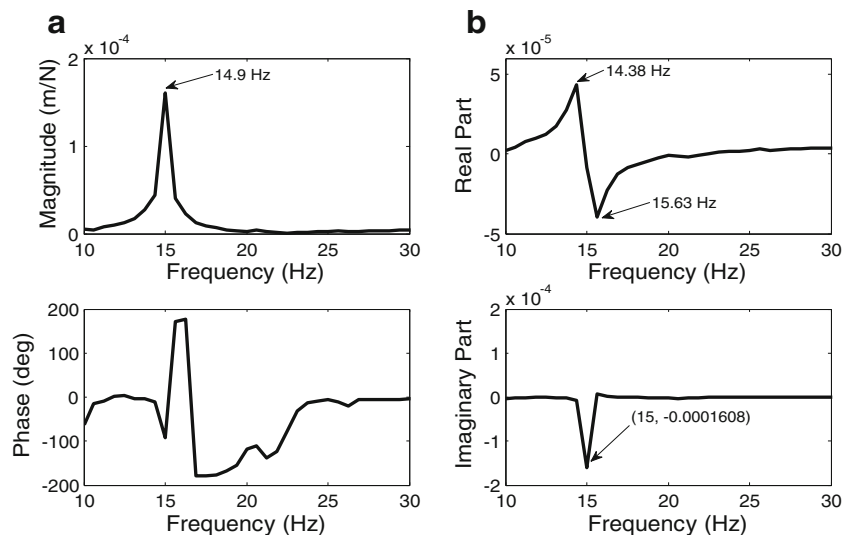
Fig. 9 Bode diagrams TF_1, TF_2, TF_3, and closed position loop

<div style="display: flex">

Im$_{min} = \frac{-1}{2k_2\xi_3} = -0.0001608$.   T h e r e f o r e , $k_2 = 3.7060 \cdot 10^4$ N/m.

To calculate the modal mass of the flexible mass, $m_3 = \frac{k_2}{\omega_2{}^2}$ $= \frac{k_2}{(2\pi f_2)}{}^2$, thus $m_3 = 4.22$ kg.

Considering Eq. (4), Eq. (5), Eq. (9), Eq. (10), the value calculated of the relative damping ξ_3, and the values in Table 2, the damping coefficients c_1 and c_2 will be 16,789 and 11.80 Ns/m.

4.3 Frequency analysis, transfer functions, and modes

The result of the modal analysis of the two dof model is that the natural frequency of the second mode is 85.1 Hz, while the frequency of the second and third modes of the three dof model are 15.1 and 85.65 Hz. In the second mode, it can be seen in the effect of the resonance of the flexible mass and in the third mode the vibration of the transmission.

From left to right, in Fig. 9, the primary transfer function (TF_1) for the two and three dof model, the secondary transfer function TF_2 of both models, and the tertiary transfer function TF_3 of the three dof model are shown. Finally, the closed position loop TF of the two and three dof models and the closed position loop together with the tertiary TF are compared. The influence of the structural compliance of the plate is TF_1 and TF_2, where at 15 Hz, there are changes in magnitude and phase. Also, the closed position loop TFs of the two and three dof are practically equal. However, when the tertiary TF is added to the closed position loop of the three dof model,

the peak at 15 Hz has a strong influence that will result in the appearance of overshoot and vibrations due to the inertial forces, even reducing the bandwidth of the drive.

5 Experimental validation

The validation of the model has been performed on the test bench assembly of Fig. 6. Internal and external data have been collected. The internal data have been the commanded position, the following error measured by the table linear encoder, the motor torque and velocity. These data have been collected by the oscilloscope function of the Fagor NC. The external data is the position of a retroreflector attached to the compliant mass, measured by a laser-interferometer HP 5529A with submicrometer precision and sampled by the HP 10474A metrology software [19]. All the signals have been sampled with a 4-ms period.

5.1 Time domain signals

The tests consisted on several linear motions with a square sine velocity profile with a variable length of 20, 100, and 400 mm and feed rates of 7, 15, and 30 m/min. Some results are shown in Fig. 10. There, the dashed line is the simulated position or following error in the table, continuous thick line is the measured position or following error in the table, dashed-dot line is the simulated position and following error in the

</div>

Fig. 10 Position and following error curves to several working conditions. From top to bottom: **a** V_f = 30,000 mm/min and Δx = 400 mm, **b** 30,000 mm/min and 100 mm, **c** 15,000 mm/min and 100 mm, **d** 7000 mm/min and 100 mm, and **e** 7000 mm/min and 20 mm
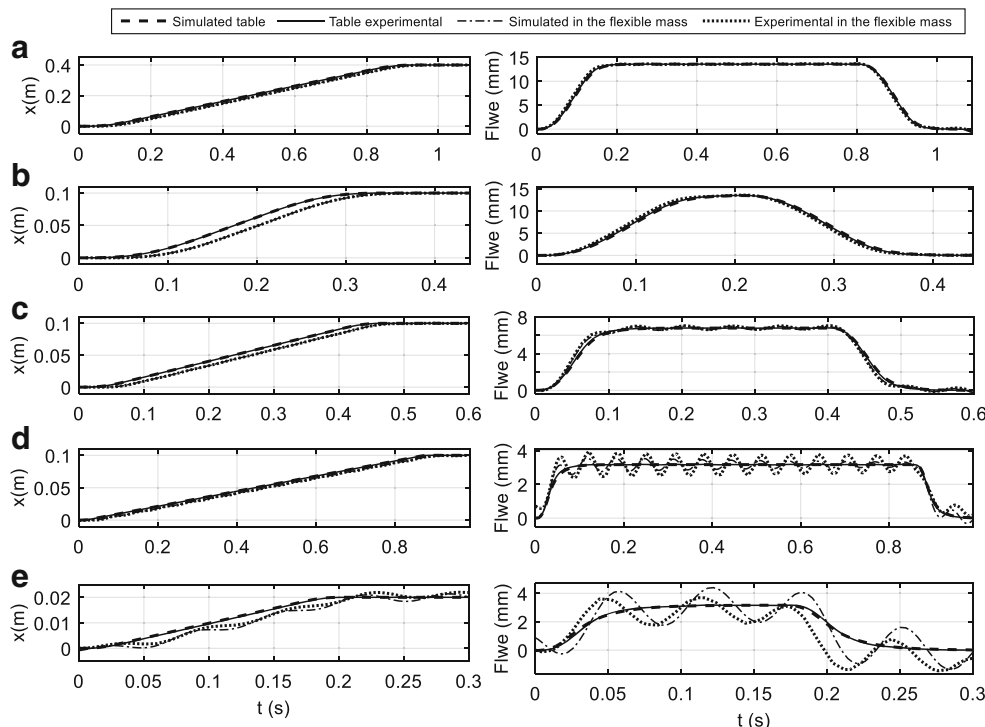
compliant mass, and the continuous thin line is the measured position and following error in the mass.

Generically, it is observed that the model curves fit well with the experimental, ones as in the case of Fig. 10a. Due to the shorter travel, which means higher frequency content in the motion, in Fig. 10c, Fig. 10d, and Fig. 10e, higher oscillations are observed in the following error of the flexible mass. This is due to the inertia and limited rigidity of the structural element. Oscillations in the following error in Fig. 10d are higher because at that shaft speed, the axis is working near the first natural frequency (15 Hz). At the same feed rate and a shorter stroke, case Fig. 10e, the oscillations in the flexible element are greater, even noticeable on the position curve.

Generally, a short and high feed rate stroke is more likely to get to work near the natural frequency (15 Hz) and get larger oscillations and overshoots, but it is not the only factor. The harmonic content of the motion actually influences the tracking error and the overshoot and that depends on the feed rate, stroke, profile shape, and acceleration time. Therefore, even programming a slower feed rate with the same stroke, Fig. 10c, greater oscillations in the following error may appear. In Fig. 11, it is seen with greater detail the comparison of the simulated and measured following error of the table; as in Fig. 10, it can be hardly seen.

In Fig. 11 again, the signals are very similar. The main difference is the amplitude of the oscillations, which seems to be higher in the simulation of the flexible mass motion but lower in the simulated table motion. This is probably due to an imperfect estimation of the damping of both the transmission chain and the compliant mass, or even due to the fact that probably the proportional damping hypothesis assumed has its limitations comparing with the experimental evidence.

Fig. 11 Following error in the table and flexible mass. V_f = 7000 mm/min and Δx = 100 mm
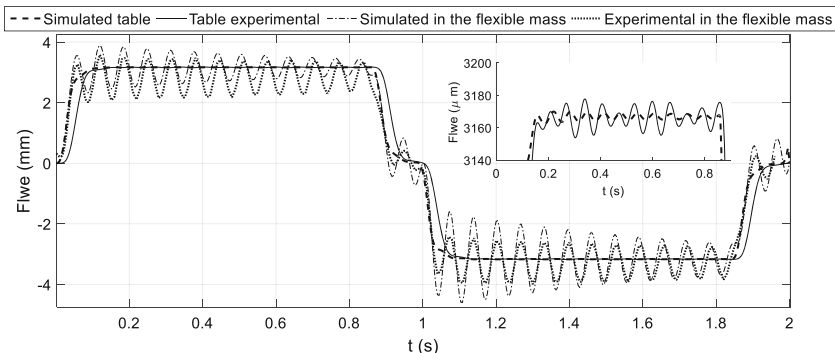
5.2 Compliant mass and table overshoot vs. maximum commanded jerk

Here, several tests have been done varying the commanded jerk of the motion profile and measuring the resulting overshoot on the drive table and the compliant mass. The measuring system is the same as in the previous section. The idea is to verify experimentally how the jerk together with the system compliance affects the overshoot of the system.

As the motion profile is a velocity square sine, to change the commanded jerk, first, the equations of the motion have to be developed. In this motion profile, the acceleration time t_{acc} is the time needed to reach the fast positioning speed $G0$ of the drive. Deriving the velocity equation, the following commands in acceleration and jerk are obtained; see Eq. (15), where V_f is the feed rate:

$$a(t) = \frac{\pi \cdot G0}{2 \cdot t_{acc}} \cdot \sin\left(\frac{\pi \cdot G0}{V_f \cdot t_{acc}} t\right). \qquad\qquad j(t) = \frac{1}{2 \cdot V_f}\left(\frac{\pi \cdot G0}{t_{acc}}\right)^2 \cdot \cos\left(\frac{\pi \cdot G0}{t_{acc} V_f} \cdot t\right). \qquad (15)$$

Thus, the maximum acceleration and jerk values correspond to the following:

$$a_{max} = \frac{\pi \cdot G0}{2 \cdot t_{acc}}. \qquad\qquad j_{max}$$

$$= \frac{1}{2 \cdot V_f}\left(\frac{\pi \cdot G0}{t_{acc}}\right)^2 = \frac{2(a_{max})^2}{V_f}. \qquad (16)$$

Hence, varying the acceleration time of the profile, the demanded acceleration, and jerk can be changed. Here, several acceleration times from 60 to 300 ms have been tested, which means that a maximum jerk of 1370, 771, 610, 493, 216, 124, 79, 63, and 54 m/s^3 have been tested. The feed rate has been set at 15 m/min, and the stroke is 590 mm. The measured overshoot values on the table and flexible mass are compared with the simulated ones in Fig. 12a and Fig. 12b, respectively. Regarding the simulations, the overshoots calculated with the whole mechatronic model are plotted but also as a reference, the displacements obtained considering only the transmission TFs as in Section 3 are shown.

Comparing the overshoots simulated with the mechatronic model and the experimental ones, it can be said that there is a reasonable agreement. In Fig. 12b all the tests are above the predicted trend, while in Fig. 12a, the measured overshoots seem to be always higher than the predicted ones, which again can be due to a poor damping identification. Although the expected trend was an increase of the overshoot with the commanded jerk, the experimental results and the model show that there are several jerk values where the overshoot decays, as at 54 and 124 m/s^3 in Fig. 12b. At those values, it seems that the demanded jerk together with the profile shape and the system dominant natural frequency result in a cancelation of the compliant mass vibration. This is an interesting effect that will be further analyzed.

Comparing the predictions of the mechatronic model and the transmission models, it is clear that the position control task means a lower overshoot as predicted by the mechatronic model. However, it must be noted how the shape of the simulated curves is similar in Fig. 12b, but not in Fig. 12a. This is explained again by the dominant frequencies of the simulated

Fig. 12 Table and flexible mass overshoot Δs depending on the commanded maximum jerk
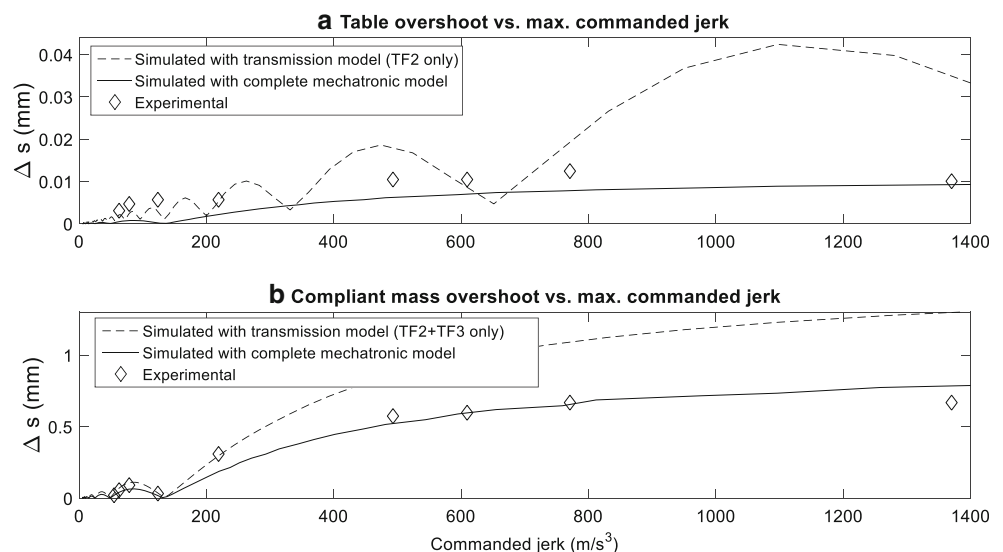
systems. In Fig. 12b, the dominant frequency of the transmission, TF_2 and TF_3, is the same as the closed position loop, that is, 15.3 Hz, see Fig. 9. In Fig. 12a, the shape is different because the TF_2 dominant frequency is 56.5 Hz, different from the dominant frequency of the closed position loop. The result is that with the transmission model only, the jerk values that minimize the overshoot are higher.

On the other hand, the drive precision without compliant mass was calculated by means of ISO 230–2 norm [20], as in the tests performed by Castro and Burdekin [21, 22]. According to the standard, the precision of the drive is 8 μm. However, when the mass is attached, to keep the compliant mass overshoot equal to or below 8 μm, the maximum commanded jerk must be below 20 m/s^3. If a two dof model was considered, an erroneous maximum jerk of 200 m/s^3 would be estimated. That is, the decrease of the maximum jerk for an overshoot of 8 μm is from 200 to 20 m/s^3, a 90 %. Hence, this methodology could be used by a customer who needs to know the maximum jerk to command for a given overshoot at the table or the tool tip.

6 Conclusions

The contributions of the present work are the following:

First, a three dof mechatronic model integrating the dynamics of the transmission chain, the structural elements of large machine tools, and the cascaded control of position, velocity, and current. All the formulation is provided for the three dof model, that is, the required transfer functions and the damping coefficients analytical expressions. The model has been programmed and used to simulate the influence of the machine structural element compliance which results in a different displacement at the tool tip suffers compared to the displacement measured by the control at the linear encoder.

The model developed has been used also to estimate the maximum commanded jerk that a machine tool can execute without excessive overshoot at the tool tip. The comparisons made show that the error in the estimation of the maximum jerk when the machine compliance is ignored can be up to 90 %.

A test bench consisting on a ball screw drive and a compliant mass that simulates the compliance of a large machine has been used for experimental testing. Several experimental tests with variable feed rates and strokes show a good agreement with the model, although there is room for improvement in the damping values estimation.

Also, to analyze the variation of the mass overshoot with the maximum commanded jerk, several tests have been done, measuring the displacement with a linear interferometer. The results show a good agreement with the model predictions. What is more, although it is expected to find a higher overshoot as the jerk increases, it has been shown how there exist some jerk values where the resulting overshoot is minimized. The location of those values seems to have a relation with the motion profile and specially, with the dominant frequency of the system. That means that it could be possible to program a minimum overshoot jerk for each motion, although this has to be further analyzed.

To conclude, a tool capable of simulating different test drives of any structural element in the design stage, reducing the trial and error stage, and avoiding the necessity of building large and expensive prototypes is presented.

Appendix 1

Modal matrix

The modal matrix is initially obtained as

$$[\phi] = \begin{bmatrix} 1 & 1 & 1 \\ 1 & 1-\dfrac{\omega_2^2}{(\omega_{1r23})^2} & 1-\dfrac{\omega_3^2}{(\omega_{1r23})^2} \\ & 1-\dfrac{\omega_2^2}{(\omega_{1r23})^2} & 1-\dfrac{\omega_3^2}{(\omega_{1r23})^2} \\ 1 & 1-\dfrac{\omega_2^2}{(\omega_{3r12})^2} & 1-\dfrac{\omega_3^2}{(\omega_{3r12})^2} \end{bmatrix}. \quad (17)$$

After normalization with respect to the mass matrix, the $[\varphi]$ modal matrix is

$$[\phi] = \begin{bmatrix} \dfrac{1}{\sqrt{m_T}} & \dfrac{1}{a_1} & \dfrac{1}{a_2} \\[2mm] \dfrac{1}{\sqrt{m_T}} & \dfrac{1-\dfrac{\omega_2^2}{\omega_{1r23}^2}}{a_1} & \dfrac{1-\dfrac{\omega_3^2}{\omega_{1r23}^2}}{a_2} \\[2mm] \dfrac{1}{\sqrt{m_T}} & \dfrac{1-\dfrac{\omega_2^2}{\omega_{1r23}^2}}{\left(1-\dfrac{\omega_2^2}{\omega_{3r12}^2}\right)a_1} & \dfrac{1-\dfrac{\omega_3^2}{\omega_{1r23}^2}}{\left(1-\dfrac{\omega_3^2}{\omega_{3r12}^2}\right)a_2} \end{bmatrix}. \quad (18)$$

The a_1 and a_2 constant terms of Eq. (18) simplify the modal matrix expression. These are defined in Eq. (19).

$$a_1 = \sqrt{\dfrac{\left(m_3\omega_{3r12}^4 + m_2\left(\omega_2^2-\omega_{3r12}^2\right)^2\right)\left(\omega_2^2-\omega_{1r23}^2\right)^2}{\left(\omega_2^2-\omega_{3r12}^2\right)^2\omega_{1r23}^4} + m_1}.$$

$$a_2 = \sqrt{\dfrac{\left(m_3\omega_{3r12}^4 + m_2\left(\omega_3^2-\omega_{3r12}^2\right)^2\right)\left(\omega_3^2-\omega_{1r23}^2\right)^2}{\left(\omega_3^2-\omega_{3r12}^2\right)^2\omega_{1r23}^4} + m_1}.$$

$$(19)$$

Appendix 2

Equations for stiffness

Then, equations to determine the values of torsional, axial, and bending rigidity are presented. These will be function of the shear modulus G, the torsional moment of inertia J, the bar length L, the Young's modulus E, the area of the cross-section A, and the axial moment of inertia I.

$$k_{\text{torsional}} = \frac{G \cdot J}{L} \quad k_{\text{axial}} = \frac{E \cdot A}{L} \quad k_{\text{flexure}} = \frac{3E \cdot I}{L^3} \quad (20)$$

Appendix 3

Being "p" the screw pitch, the resulting stiffness between servomotor and the loading part in the two dof model or transmission part in the three dof model is

$$\frac{1}{k_1} = \frac{1}{k_{em}\left(\frac{2\pi}{p}\right)^2} + \frac{1}{k_{AF}\left(\frac{2\pi}{p}\right)^2} + \frac{1}{\left(k_{Ht}\left(\frac{2\pi}{p}\right)^2 + k_{Ha}\right)}$$
$$+ \frac{1}{k_T} + \frac{1}{k_M}. \quad (21)$$

Thus, by inverse, the equivalent rigidity k_1 is obtained as follows:

$$k_1 = \left[\frac{1}{k_{em}\left(\frac{2\pi}{p}\right)^2} + \frac{1}{k_{AF}\left(\frac{2\pi}{p}\right)^2} + \frac{1}{\left(k_{Ht}\left(\frac{2\pi}{p}\right)^2 + k_{Ha}\right)} + \frac{1}{k_T} + \frac{1}{k_M}\right]^{-1}. \quad (22)$$

The unit transformation from the inertia to mass is direct in the case of the servomotor:

$$m_1 = J_m\left(\frac{2\pi}{p}\right)^2 \quad (23)$$

To reduce the mass of the transmission part in the three dof model or load part in the case of two dof model, which includes the inertia of the coupling, screw, nut, and table, it is obtained by

$$m'_2 = J_{AF1}\left(\frac{2\pi}{p}\right)^2 + J_{AF2}\left(\frac{2\pi}{p}\right)^2 + J_H\left(\frac{2\pi}{p}\right)^2 + m_T$$
$$+ m_M. \quad (24)$$

It should be taken into account that an aluminum block of 9.15 kg is added at the table, which will support and assembly the set of the flexible mass, therefore:

$$m_2 = m'_2 + 9.15. \quad (25)$$

References

1. Zulaika JJ, Campa FJ, Lopez de Lacalle LN (2011) An integrated process–machine approach for designing productive and light-weight milling machines. Int J Mach Tools Manuf 51(7–8):591–604
2. Uriarte L, Zatarain M, Axinte D, Yagüe-Fabra J, Ihlenfeldt S, Eguia J, Olarra A (2013) Machine tools for large parts. CIRP Ann - Manuf Technol 62(2):731–750
3. Gomez-Acedo E, Olarra A, Zubieta M, Kortaberria G, Ariznabarreta E, López de Lacalle LN (2015) Method for measuring thermal distortion in large machine tools by means of laser multilateration. Int J Adv Manuf Technol 80(1–4):523–534
4. Fernandez-Gauna B, Ansoategui I, Etxeberria-Agiriano I, Graña M (2014) Reinforcement learning of ball screw feed drive controllers. Eng Appl Artif Intell 30:107–117
5. Dequidt A, Castelain J-M, Valdès E (2000) Mechanical pre-design of high performance motion servomechanisms. Mech Mach Theory 35(8):1047–1063
6. Altintas Y, Verl A, Brecher C, Uriarte L, Pritschow G (2011) Machine tool feed drives. CIRP Ann. - Manuf. Technol. 60(2):779–796
7. Caracciolo R, Richiedei D (2014) Optimal design of ball-screw driven servomechanisms through an integrated mechatronic approach. Mechatronics 24(7):819–832
8. Neugebauer R, Ihlenfeldt S, Frieß U, Wabner M, Rauh S (2012) New high-speed machine tool structure by holistic mechatronic systems design. Procedia CIRP 1:307–312
9. Wu S-T, Lian S-H, Chen S-H (2015) Vibration control of a flexible beam driven by a ball-screw stage with adaptive notch filters and a line enhancer. J Sound Vib 348:71–87
10. Fortunato A, Ascari A (2013) The virtual design of machining centers for HSM: towards new integrated tools. Mechatronics 23(3):264–278
11. Zulaika JJ, Ander Altamira J (2005) Diseño mecatrónico de servomecanismos de alta dinámica. Automática E Instrum 5(362):59–64
12. Gross H, Hamann J, Wiegärtner G (2001) Electical feed drives in automation: basics, computation, dimensioning. Publicis MCD Corporate Pub, Erlangen
13. Ellis G (2004) Control system design guide. Elsevier Academic Press, Amsterdam
14. Vicente DA, Hecker RL, Villegas FJ, Flores GM (2011) Modeling and vibration mode analysis of a ball screw drive. Int J Adv Manuf Technol 58(1–4):257–265
15. Blevins RD (1979) Formulas for natural frequency and mode shape. Van Nostrand Reinhold Co, New York
16. Chen CL, Jang MJ, Lin KC (2004) Modeling and high-precision control of a ball-screw-driven stage. Precis Eng 28(4):483–495
17. Erkorkmaz K, and Altintas Y, (2001) High speed CNC system design. Part II: modeling and identification of feed drives.
18. Magnani G, Rocco P (2010) Mechatronic analysis of a complex transmission chain for performance optimization in a machine tool. Mechatronics 20(1):85–101
19. Usop Z, Sarhan AAD, Mardi NA, Wahab MNA (2015) Measuring positioning, circularity and static errors of a CNC vertical machining Centre for validating the machining accuracy. Meaurement 61:39–50
20. (2000) ISO 230–2. Determination of accuracy and repeatability of positioning numerically controlled axes.
21. Castro HF, Burdekin M (2003) Dynamic calibration of the positioning accuracy of machine tools and coordinate measuring machines using a laser interferometer. Int J Mach Tools Manuf 43(9):947–954
22. Castro HFF, B.urdekin M (2005) Evaluation of the measurement uncertainty of a positional error calibrator based on a laser interferometer. Int J Mach Tools Manuf 45(3):285–291